

# Microsecond-lived quantum states in a carbon-based circuit driven by cavity photons

B. Neukelmance,<sup>1,2,\*</sup> B. Hue,<sup>1,2,\*</sup> Q. Schaeverbeke,<sup>2</sup> L. Jarjat,<sup>1</sup> A. Théry,<sup>1</sup> J. Craquelin,<sup>1</sup>  
 W. Legrand,<sup>1,2</sup> T. Cubaynes,<sup>1</sup> G. Abulizi,<sup>2</sup> J. Becdelievre,<sup>2</sup> M. El Abbassi,<sup>2</sup> A. Larrouy,<sup>2</sup> K.F. Ourak,<sup>2</sup>  
 D. Stefani,<sup>2</sup> J.A. Sulpizio,<sup>2</sup> A. Cottet,<sup>1,3</sup> M.M. Desjardins,<sup>2</sup> T. Kontos,<sup>1,3,†</sup> and M.R. Delbecq<sup>1,3,4,†</sup>

<sup>1</sup>*Laboratoire de Physique de l'École normale supérieure, ENS, Université PSL,  
 CNRS, Sorbonne Université, Université Paris Cité, Paris, France*

<sup>2</sup>*C12 Quantum Electronics, Paris, France*

<sup>3</sup>*Laboratoire de Physique et d'Etude des Matériaux, ESPCI Paris,  
 Université PSL, CNRS, Sorbonne Université, Paris, France*

<sup>4</sup>*Institut universitaire de France (IUF)*

Semiconductor quantum dots are an attractive platform for the realisation of quantum processors. To achieve long-range coupling between them, quantum dots have been integrated into microwave cavities. However, it has been shown that their coherence is then reduced compared to their cavity-free implementations. Here, we manipulate the quantum states of a suspended carbon nanotube double quantum dot with ferromagnetic contacts embedded in a microwave cavity. By performing quantum manipulations via the cavity photons, we demonstrate coherence times of the order of 1.3  $\mu$ s, two orders of magnitude larger than those measured so far in any carbon quantum circuit and one order of magnitude larger than silicon-based quantum dots in comparable environment. This holds promise for carbon as a host material for spin qubits in circuit quantum electrodynamics.

Spins isolated in nano-scale devices are a well-established platform for solid-state quantum information processing [1, 2]. Although elementary multi-qubit systems have been implemented, scaling spin qubit architectures remains an outstanding challenge despite the progress made in recent years [3–5]. The hardware problem at stake in this endeavor constantly triggers the search for new materials and new architectures [6].

One promising architecture, borrowed from superconducting qubits, combines isolated spins and microwave cavity photons in a circuit quantum electrodynamics (cQED) setup [7–14]. The methods used in this context are very appealing for upscaling spin qubit processors. Recent breakthroughs towards this goal include the use of high-impedance cavities to enhance the spin-photon coupling [9, 13], which has led to the first implementation of a two-qubit gate between distant spins [14]. However, the coherence times observed for spins in cavities are essentially two orders of magnitude smaller than their cavity-free implementations, limiting the single- and two-qubit gate fidelities.

Among the many potential solutions, carbon nanotubes have shown great promise [15, 16]. In principle, carbon nanotube-based circuits display many attractive features: they can form well-defined and tunable quantum dots [16], they can be suspended, reducing impact of stray charges, and they can be grown with pure <sup>12</sup>C, offering a nuclear spin-free environment for electronic spin qubits. However, so far they have only been shown to host quantum states with limited coherence of the order of 10 ns [17, 18].

In this work, we show that carbon nanotube-based quantum devices finally hold to their promise and can

serve as an alternative to existing platforms. Our setup displays several features which compare favorably with the state-of-the-art. First, we demonstrate coherent control of quantum states in a carbon nanotube circuit with a coherence time longer by about 2 orders of magnitude than previously observed [17, 18]. Second, we are able to perform all the basic operations of our carbon-based circuit at zero external magnetic field and elevated temperature  $T \approx 300$  mK compared to the driving frequency  $f_d \approx 9$  GHz. Third, the quantum states are solely controlled by cavity photons, which fully exploits the possibilities of cQED. Finally, the coherence time of approximately 1.3  $\mu$ s is the largest reported for quantum dots in cavities for any material.

In order to address long-lived quantum states in a carbon-based circuit via cQED techniques, a spin-photon coupling is engineered [7]. A suspended carbon nanotube is connected to ferromagnetic electrodes with non-collinear magnetizations and coupled electrostatically to five gate electrodes. One of those is directly connected to the central conductor of a coplanar waveguide (CPW) microwave resonator to induce charge-photon coupling. Additionally, the ferromagnetic electrodes polarize locally the spectrum of the carbon nanotube [19] which induces a synthetic spin-orbit interaction enabling spin-photon coupling [7]. This is illustrated in the panel a of figure 1. A typical device layout is shown in panels b, c and d. The CPW cavity, visible in panel b, is made out of a 100 nm layer of Nb. Its fundamental resonance frequency at 300 mK is  $f_c = 6.975$  GHz with a quality factor  $Q = 4853$ . A close-up on the location of the double quantum dot is shown in panel c. Large trenches are made for the final integration of the carbon nanotube [11, 20]. The zig-zag shaped ferromagnetic electrodes are designed for creating the non-collinear magnetization and can be seen in panel d on either side of the gates. The ferromagnetic electrodes are made with

\* These two authors contributed equally to this work.

† These two authors co-supervised the project.

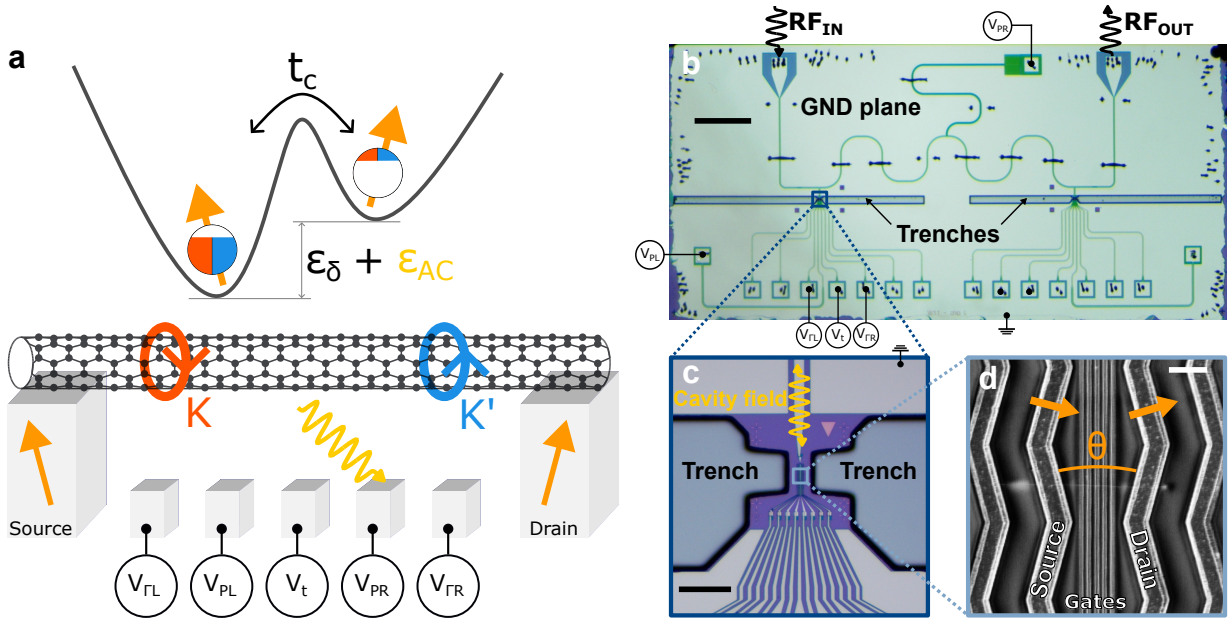


**FIG. 1. Schematic and images of the device.** **a.** Schematic of the device. A carbon nanotube is suspended above 5 DC gates and connected to ferromagnetic contacts. The gates allow to form a double well potential in order to trap an electron.  $\epsilon_\delta$  represents the depth asymmetry between the two wells. The electron can tunnel from one well to the other at a rate  $t_c$ , thus its wave function is delocalized over the two wells as represented by the filling of each circle. The non-collinear ferromagnetic electrodes impose a different spin quantization axis in each well as shown by the orange arrows. In addition, the electron can be in either valley  $K$  (red) or  $K'$  (blue). Finally the circuit is coupled to a microwave cavity via the gate  $V_{PR}$  which is connected to the central track of the coplanar waveguide resonator, thus inducing a modulation  $\epsilon_{AC}$  on the energy detuning between the two wells. **b.** Optical image of the sample. On the upper part, the coplanar waveguide resonator is connected to two ports. The IN port is used to both fill the cavity and drive the nanotube circuit. The OUT port is used for reading-out the cavity. In the middle, there are the trenches used to deposit the carbon nanotube. On the bottom part, there are the DC lines used to form the double well potential. The bar is 1 mm. **c.** Optical image of a nanotube transfer region showing the large scale view of the electrodes. The scale bar is 50  $\mu\text{m}$ . **d.** Scanning electron microscope image of a typical device with a nanotube transferred onto the ferromagnetic electrodes and suspended over the gates. The bar is 1  $\mu\text{m}$  and  $\theta = \pi/6$ .

a Ti(185 nm)/Ni<sub>80</sub>Pd<sub>20</sub>(35 nm)/Pd(4 nm) stack whereas the gates are made with a Ti(5 nm)/Pd(50 nm) stack. The gate electrodes having a conducting surface ensure that we can check electrically on the final device that the nanotube is suspended and well isolated from the gates. At the very last step of the nano-fabrication process, a nano-scale transfer of a nanotube grown on a comb via a CH<sub>4</sub> based chemical vapor deposition process is performed. It leads to device resistances between 0.5 M $\Omega$  and 20 M $\Omega$  at room temperature. The particular device studied here had a room temperature resistance of about 8 M $\Omega$ .

All the measurements presented in this paper have been made at 300 mK. Note that this is an order of magnitude larger than conventional qubit operating temperatures, which has recently been shown to be favorable for mitigating heating from microwave drive [21], however we are not in the “hot” qubit regime [22, 23]. The main features of our device can be first characterized via DC transport measurements and continuous wave spectroscopy. The corresponding measurements are shown in figure 2. Panel a shows the phase shift of the microwave tone sent at  $f_c$  as a function of the two plunger gate volt-

ages, in the region of interest in this work. We observe the microwave signal characteristic of the transition between two adjacent charge states. In panel b, the DC current as a function of the magnetic field applied perpendicularly to the nanotube axis is shown for different working points on the closest bias triangles where significant current is measurable. A gate dependent hysteretic signal in the current is observed. It validates spin injection [7, 24] and therefore the presence of interface exchange fields. Turning to two-tone spectroscopy, we present in panel c the phase contrast probed at  $f_c$  as a function of the continuous drive frequency  $f_d$ . The drive tone is applied via the cavity at an input power  $P_d = -54$  dBm (uncalibrated). A resonance is found at  $f_r = 9.0987$  GHz with a linewidth of 589 kHz extracted from the Lorentzian fit shown as an orange line in panel c. Furthermore, we observe that the resonance frequency varies with respect to the energy detuning  $\epsilon_\delta$  between the left and right plunger gates, as shown in panel d, confirming that it is a transition of the double quantum dot spectrum. The observed dispersion is strikingly small, a few MHz over hundreds of GHz for  $\epsilon_\delta$ , yet it is well captured by the theory as shown by the white dashed line (Supplementary Information).

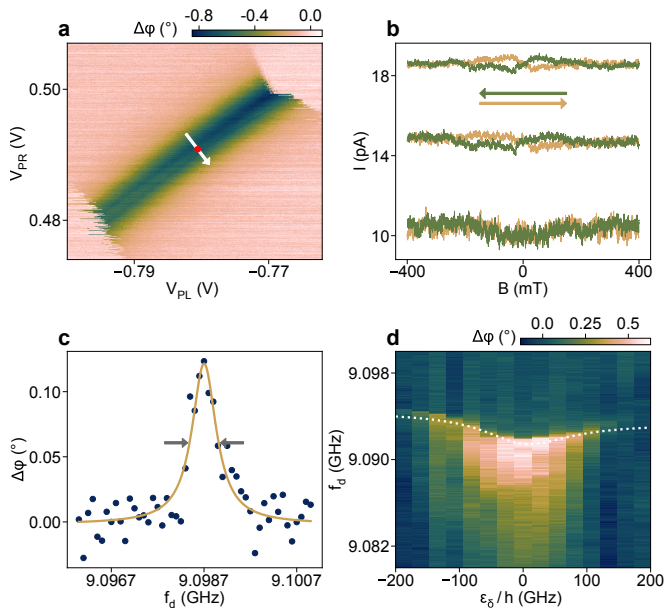


FIG. 2. **Spectroscopy and magnetic hysteresis of the circuit.** **a.** Continuous wave spectroscopy of the interdot transition studied in the paper. The measured signal is the phase of the microwave signal at  $f_c$  as a function of the left and right plunger gate voltages. The arrow indicates the  $\epsilon_\delta$  axis presented in panel d. The red dot displays the working point  $\epsilon_\delta = 0$  at which the continuous spectroscopy and the time domain measurements are performed. **b.** Transport measurements as a function of the magnetic field showing the characteristic hysteretic magnetoresistance. The arrows indicate which way the magnetic field was swept for each curve. The three pairs of curves correspond to three different plunger gates settings. **c.** Two-tone microwave spectroscopy as a function of  $f_d$  showing a resonance at  $f_r = 9.0987$  GHz. The Lorentzian fit yields a linewidth of 589 kHz. The grey arrows indicate the full width at half maximum. **d.** Dispersion of the resonance frequency with respect to the energy detuning  $\epsilon_\delta$ . The white dashed line is the dispersion predicted by our model.

This small dispersion indicates that low charge noise dephasing can be achieved. Overall, these measurements validate that we have indeed implemented the scheme presented in figure 1a.

Going to the time domain is crucial to further understand the spectrum and the dynamics of our system. We first perform Rabi oscillations. For this purpose, we excite the system with a frequency  $f_d$  close to the resonance found in figure 2c and for a burst time  $t_{\text{burst}}$  up to 2  $\mu\text{s}$ , by steps of 20 ns. Right after, we read-out the resulting system state using a second pulse at  $f_c$  (Supplementary Information). The corresponding measurement is shown in figure 3a. We observe fringes signaling quantum oscillations. These fringes resemble conventional Rabi chevrons observed in many qubit experiments and extend up to almost 2  $\mu\text{s}$ . However, there are two main differences here. First, the chevrons for  $f_d > 9.0970$  GHz oscillate slightly slower than those for  $f_d < 9.0970$  GHz.

Second, there is a horizontal stripe with almost no oscillation contrast very close to the resonance. Nevertheless, the cut at  $f_d = 9.0984$  GHz shown in figure 3b displays well-defined damped oscillations which we fit with an exponentially decaying cosine. We extract a Rabi frequency  $\Omega_R/(2\pi) = 2.51$  MHz and a Rabi decay time  $T_{\text{Rabi}} = (0.59 \pm 0.05)$   $\mu\text{s}$ .

The Rabi chevrons pattern is very sensitive to the spectrum of the probed system. In particular, our unconventional chevrons pattern tends to indicate a multi-level dynamics [25]. Furthermore, we observe that the Rabi frequency  $\Omega_R$  scales as  $A_d^{2/3}$  with  $A_d$  the drive amplitude (figure 3c). This scaling strongly points to the dynamics associated with a quasi-harmonic spectrum [26]. In the simplest picture of a single particle Hamiltonian with two orbital states  $|L\rangle$  and  $|R\rangle$  for left and right dot occupancy, two spin states  $|\uparrow\rangle$  and  $|\downarrow\rangle$ , and the two valley states  $|K\rangle$  and  $|K'\rangle$  inherited from the carbon nanotube band structure, the double quantum dot spectrum is made up of 8 levels from which two gapped 4-levels quasi-harmonic ladder can be formed, as illustrated in figure 3e. We find indeed that with experimentally reasonable parameters, we can account for both the small dispersion with detuning  $\epsilon_\delta$  of the transition, as shown by the white dotted line in figure 2d, and reproduce very well the peculiar Rabi chevrons, as shown in figure 3d (Supplementary Information). The corresponding spectrum is shown in figures 3e and 3f. It is calculated with the angle  $\theta$  between the ferromagnetic contacts set to its lithographically designed value of  $\pi/6$ , intervalley couplings of the order of 4.5 GHz, exchange fields  $E_{L/R}^Z/h$  on the left and the right dots between 9 and 10 GHz, a large tunnel coupling  $t_c/h \approx 31$  GHz and a bare charge-photon coupling of  $g_0/(2\pi) \approx 27$  MHz. The small intervalley couplings indicate that our nanotube is very clean [16]. Having the intervalley couplings smaller than the exchange fields is essential to obtain the small dispersion in detuning. With these parameters, all eigenstates of the spectrum are fully hybridized between charge, spin and valley at zero detuning. Despite this, the transitions between states  $|0\rangle$  and  $|1\rangle$  and between states  $|2\rangle$  and  $|3\rangle$  are valley transitions. It is confirmed by an almost flat dispersion of the transition with external magnetic field applied perpendicularly to the nanotube axis both in experiment and the simulation (Supplementary Information). All other transitions would be spin-valley transitions similar to previously manipulated spin-valley qubits [17, 18]. In addition, this model and parametrization predicts the coupling of each transition to the cavity mode. By applying a common drive amplitude coefficient, we can thus match the observed Rabi frequencies  $\Omega_{01}$ ,  $\Omega_{12}$  and  $\Omega_{23}$ .

Despite the multilevel dynamics, the observation of well-defined Rabi oscillations at a given drive frequency enables to measure accurately the relaxation time  $T_1$  and decoherence time  $T_2^*$  of the system. The latter is achieved by Ramsey interferometry, that is, performing two  $\pi/2$ -pulses separated by a wait time  $\tau$  and measuring the resulting state. In our case, a  $\pi/2$ -pulse is achieved in

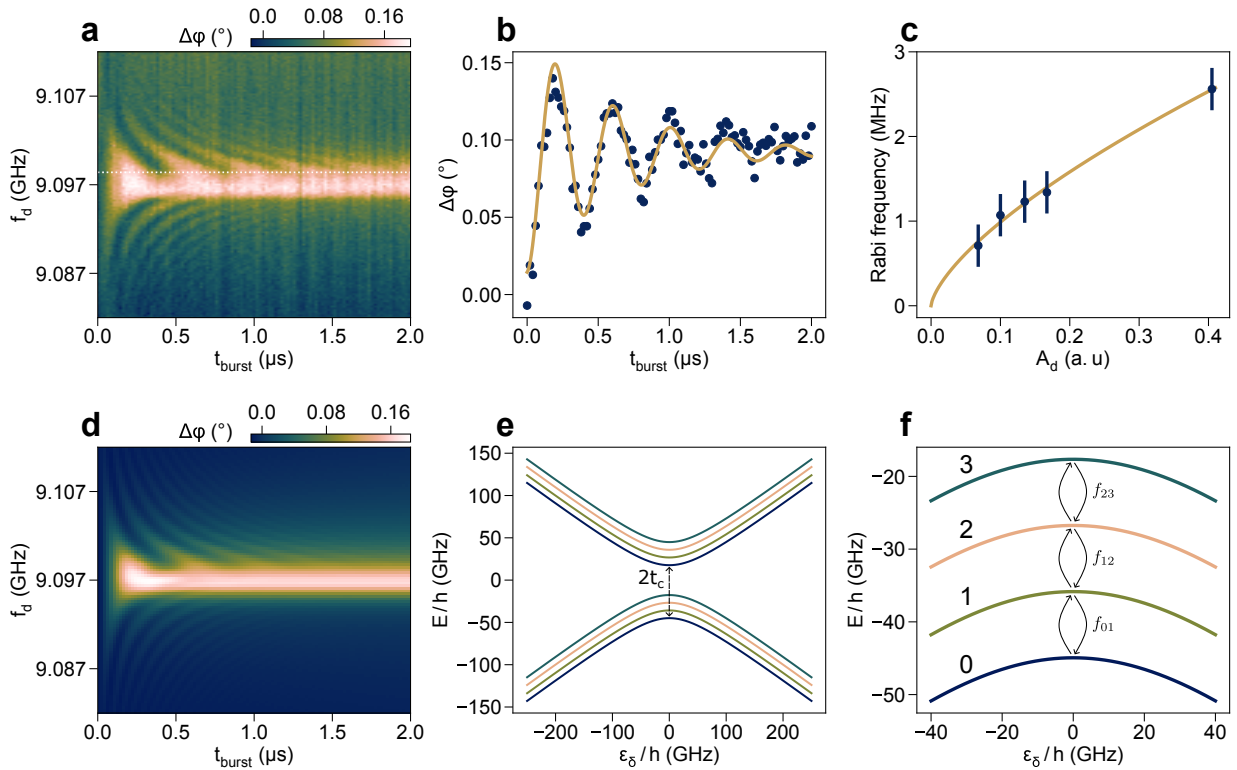


FIG. 3. **Rabi oscillations.** **a.** Rabi chevrons pattern of the carbon nanotube device. It is observed through the oscillations of the phase contrast  $\Delta\phi$  as a function of the drive frequency  $f_d$  and drive time  $t_{\text{burst}}$ . **b.** Cut in panel a at  $f_d = 9.0984$  GHz (white dashed line) showing Rabi oscillations as a function of time fitted by an exponentially decaying cosine. **c.** Dependence of the Rabi frequency as a function of the drive amplitude  $A_d$  (filled circles). The orange line is a fit to a power law  $\Omega_R \propto A_d^{2/3}$ . **d.** Simulation of the Rabi chevrons pattern of panel a. **e.** Energy spectrum used to model the Rabi chevrons. **f.** Close-up on the first four levels involved in the Rabi oscillations dynamics.

100 ns. This yields the phase contrast as a function of the drive frequency  $f_d$  and the wait time  $\tau$  shown in figure 4a. The observed fringes are reproduced in figure 4b using the same model and parameters as the one used for the Rabi chevrons. Moreover, a cut in these fringes at  $f_d = 9.0984$  GHz is fitted to a Gaussian decaying cosine which yields  $T_2^* = (1.27 \pm 0.15) \mu\text{s}$  (Supplementary Information). This is the highest reported coherence time for a state in a quantum dot in a cavity [14]. We note that despite the multilevel dynamics of our system, the Ramsey fringes are very similar to the ones of a qubit. This is further confirmed by looking at the Fourier transform (Supplementary Information) where we clearly see that the oscillations frequency depends linearly on the drive frequency detuning. In order to characterize further the dephasing mechanisms in our system, it is instructive to perform a Hahn-echo measurement for which one interleaves a  $\pi$ -pulse in between the two  $\pi/2$ -pulses of the Ramsey sequence. This is shown in figure 4c. It allows us to extend the coherence time up to  $T_{2E} = (2.02 \pm 0.21) \mu\text{s}$ , which can be considered as our  $T_2$  time. Finally, we get a complete picture of the decoherence by performing a relaxation measurement using a  $\pi$ -pulse and waiting a time  $\tau$  to measure. It yields  $T_1 = (1.12 \pm 0.06) \mu\text{s}$  (see figure 4d). The  $T_2$  time is thus not far from the  $2T_1$  limit

which hints at very slow dephasing noise.

Given that we now have all the figures of merit of our system, we can make its decoherence “budget”. Among the processes which can contribute to decoherence, we have radiative processes with the photon bath of the cavity (essentially the Purcell effect since the cavity thermal mean occupation is about 1 photon at 300 mK) and the phonon bath of the suspended nanotube, charge noise, nuclear spin noise and cotunneling arising from virtual tunneling on and off of the dots levels to the leads. The Purcell rate reads:  $\Gamma_{\text{Purcell}} = \kappa g^2 / (\omega_c - \omega_q)^2$ , where  $\kappa = \omega_c / Q$  is the mode damping rate,  $\omega_c / (2\pi)$  are the frequencies of the mode and the driven transitions respectively and  $g$  is the coupling strength between the transition and the mode. The model gives  $g / (2\pi) \leq 2.5$  MHz for all transitions involved, leading to  $\Gamma_{\text{Purcell}} / (2\pi) \leq 1.7 \times 10^{-6}$  MHz for the cavity, which is 6 orders of magnitude below the rates which we measure. Such a small value is expected given the large frequency detuning between the cavity and the transitions. The effect of charge noise can be inferred from the slope of the transition with respect to detuning which is of the order of  $4 \times 10^{-3}$  MHz/ $\mu\text{eV}$ . Taking detuning fluctuations of  $\sqrt{\langle \sigma_c^2 \rangle} \approx 10$   $\mu\text{eV}$ , typical for CNT devices in cavities [11, 27, 28], we obtain  $\Gamma_{\phi, \text{charge}} / (2\pi) \approx 4 \times 10^{-2}$  MHz,

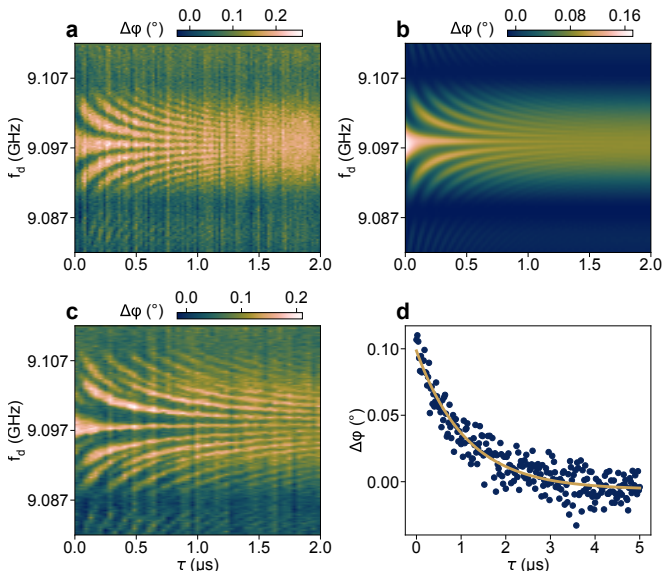


FIG. 4. **Decoherence characterization.** **a.** Ramsey fringes of the carbon nanotube device. It is observed through the oscillations of the phase contrast  $\Delta\varphi$  as a function of the drive frequency  $f_d$  and time delay  $\tau$  between the two  $\pi/2$ -pulses of duration  $\tau_{\pi/2} = 100$  ns. **b.** Simulation of the Ramsey fringes pattern of panel a using the level structure displayed in figure 3f and using the same parameters as in the figures 3d and 3e. **c.** Hahn-echo fringes. **d.** Relaxation measurement yielding  $T_1 = 1.1$   $\mu$ s.

about one order of magnitude smaller than our observations. Hyperfine interaction-mediated spin dephasing is also expected to yield small contribution with  $\Gamma_{\phi, \text{hf}}/(2\pi) \approx 4 \times 10^{-2}$  MHz. This value is slightly larger than previous estimates because they were based on formulae widely used in the literature, e.g. in ref. [11, 18], which led to an underestimation of the contribution of nuclear spins to spin dephasing in carbon nanotubes. This issue has been addressed in ref. [29]. For relaxation with phonons, as the CNT is suspended, we considered stretching modes which have a fundamental frequency  $\nu_0$  close to the transitions given by  $\nu_0 L = 12.3$  GHz  $\cdot$   $\mu$ m with  $L$  the length of the CNT in  $\mu$ m [30]. It gives  $\nu_0$  between 8.2 and 6.15 GHz for  $L$  between 1.5 and 2  $\mu$ m as designed. The Rabi chevrons and Ramsey fringes are well reproduced considering this relaxation process with a bare electron-phonon coupling of 500 MHz and a damping rate of 2.5 GHz for  $L = 1.5$   $\mu$ m (Supplementary Information). It however leads to a too small an estimation of  $T_1 \approx 0.2$   $\mu$ s indicating that it is not the main relaxation process. There remains cotunneling as a decoherence mechanism. Interestingly, it is known to contribute both to relaxation and decoherence in essentially the same way and amplitude, scaling as  $\Gamma_{\text{lead}}^2/U$  with  $\Gamma_{\text{lead}}$  the coupling to the leads and  $U$  the on-site Coulomb interaction [31]. We lack transport measurements to properly characterize cotunneling as our device

was very well isolated from the leads. However, the fact that we observed  $T_1 \approx T_2^*$  is consistent with cotunneling being the dominant source of decoherence.

By studying the peculiar Rabi chevrons pattern and the weak dispersion of the transitions' frequencies, we were able to determine the spectrum of our system. In particular, we have found that the regime with a very large tunnel coupling is favorable to strongly reduce the charge noise through a very weak dependence of the transitions' frequencies with  $\epsilon_\delta$  and  $t_c$ . We have thus demonstrated microsecond-lived quantum states in a carbon-based circuit in cQED, an order of magnitude larger than with equivalent Si-based circuits. The coherence is currently limited by  $T_1$ . Extending  $T_1$  by reducing the coupling to the leads could further boost coherence in our system to reach the pure dephasing time  $T_\varphi = (2.9 \pm 0.8)$   $\mu$ s that we estimate and which is slightly larger than in natural Si spin qubits [32]. Furthermore, all states having a spin content, it is expected that isotopically purified  $^{12}\text{C}$  nanotubes would yield even larger coherence times. Finally, combining the achieved regime with a high-impedance resonator to enhance the bare charge-photon coupling should, in future work, enable high-fidelity single- and two-qubit gates far from the Purcell limit.

**Acknowledgements:** We acknowledge fruitful discussions with Z. Leghtas, L. Bretheau and J. D. Pillet. This work is supported by the ANR MITIQ and ANR JCJC STOIC, the Emergence project MIGHTY of ville de Paris and the BPI project QUARBONE.

**Data availability:** The data that support the findings of this work are available from the corresponding authors upon reasonable request.

**Author contributions:** T.K. and M.R.D. designed and supervised the experiment. B.N. and B.H. performed the measurements. B.N., B.H., G.A. and J.B. fabricated the device with inputs from A.L. for the design. T.C., W.L., M.E., K.F.O., D.S., J.A.S., M.M.D., T.K. and M.R.D. contributed to the development of the CNT nano-assembly technique. L.J. and A.T. developed the acquisition protocols. B.N. B.H., Q.S., A.C., T.K. and M.R.D. analyzed the data and did the theory. B.H., Q.S. and M.R.D. did the numerical simulations. B.N., B.H., Q.S., L.J., A.T., J.C., M.M.D., T.K. and M.R.D. contributed to the discussion, interpretation and presentation of the results. B.N. B.H., T.K. and M.R.D. wrote the manuscript with inputs from all the authors.

**Corresponding authors:** Correspondence should be addressed to B. Hue (benjamin.hue@phys.ens.fr) and M.R. Delbecq (matthieu.delbecq@phys.ens.fr).

**Competing interests:** Authors affiliated with C12 Quantum Electronics have financial interest in the company. T.K. and M.R.D. declare equity interest in C12 Quantum Electronics. The remaining authors declare no competing interest.

- [1] D. Loss and D. P. DiVincenzo, Quantum computation with quantum dots, *Physical Review A* **57**, 120 (1998).
- [2] R. Hanson, L. P. Kouwenhoven, J. R. Petta, S. Tarucha, and L. M. K. Vandersypen, Spins in few-electron quantum dots, *Reviews of Modern Physics* **79**, 1217 (2007).
- [3] M. Veldhorst, J. C. C. Hwang, C. H. Yang, A. W. Leenstra, B. de Ronde, J. P. Dehollain, J. T. Muhonen, F. E. Hudson, K. M. Itoh, A. Morello, and A. S. Dzurak, An addressable quantum dot qubit with fault-tolerant control-fidelity, *Nature Nanotechnology* **9**, 981 (2014).
- [4] J. Yoneda, K. Takeda, T. Otsuka, T. Nakajima, M. R. Delbecq, G. Allison, T. Honda, T. Kodera, S. Oda, Y. Hoshi, N. Usami, K. M. Itoh, and S. Tarucha, A quantum-dot spin qubit with coherence limited by charge noise and fidelity higher than 99.9%, *Nature Nanotechnology* **13**, 102 (2018).
- [5] S. G. J. Philips, M. T. Mađzik, S. V. Amitonov, S. L. de Snoo, M. Russ, N. Kalhor, C. Volk, W. I. L. Lawrie, D. Brousse, L. Tryputen, B. P. Wuetz, A. Sammak, M. Veldhorst, G. Scappucci, and L. M. K. Vandersypen, Universal control of a six-qubit quantum processor in silicon, *Nature* **609**, 919 (2022).
- [6] G. Burkard, T. D. Ladd, A. Pan, J. M. Nichol, and J. R. Petta, Semiconductor spin qubits, *Reviews of Modern Physics* **95**, 025003 (2023).
- [7] J. J. Viennot, M. C. Dartiailh, A. Cottet, and T. Kontos, Coherent coupling of a single spin to microwave cavity photons, *Science* **349**, 408 (2015).
- [8] X. Mi, M. Benito, S. Putz, D. M. Zajac, J. M. Taylor, G. Burkard, and J. R. Petta, A coherent spin-photon interface in silicon, *Nature* **555**, 599 (2018).
- [9] N. Samkharadze, G. Zheng, N. Kalhor, D. Brousse, A. Sammak, U. C. Mendes, A. Blais, G. Scappucci, and L. M. K. Vandersypen, Strong spin-photon coupling in silicon, *Science* **359**, 1123 (2018).
- [10] A. J. Landig, J. V. Koski, P. Scarlino, U. C. Mendes, A. Blais, C. Reichl, W. Wegscheider, A. Wallraff, K. Ensslin, and T. Ihn, Coherent spin-photon coupling using a resonant exchange qubit, *Nature* **560**, 179 (2018).
- [11] T. Cubaynes, M. R. Delbecq, M. C. Dartiailh, R. Assouly, M. M. Desjardins, L. C. Contamin, L. E. Bruhat, Z. Leghtas, F. Mallet, A. Cottet, and T. Kontos, Highly coherent spin states in carbon nanotubes coupled to cavity photons, *npj Quantum Information* **5**, 1 (2019).
- [12] P. Harvey-Collard, J. Dijkema, G. Zheng, A. Sammak, G. Scappucci, and L. M. K. Vandersypen, Coherent Spin-Spin Coupling Mediated by Virtual Microwave Photons, *Physical Review X* **12**, 021026 (2022).
- [13] C. X. Yu, S. Zihlmann, J. C. Abadillo-Uriel, V. P. Michal, N. Rambal, H. Niebojewski, T. Bedecarrats, M. Vinet, É. Dumur, M. Filippone, B. Bertrand, S. De Franceschi, Y.-M. Niquet, and R. Maurand, Strong coupling between a photon and a hole spin in silicon, *Nature Nanotechnology* **18**, 741 (2023).
- [14] J. Dijkema, X. Xue, P. Harvey-Collard, M. Rimbach-Russ, S. L. de Snoo, G. Zheng, A. Sammak, G. Scappucci, and L. M. K. Vandersypen, *Two-qubit logic between distant spins in silicon* (2023), [arxiv:2310.16805](https://arxiv.org/abs/2310.16805) [cond-mat, physics:quant-ph].
- [15] D. V. Bulaev, B. Trauzettel, and D. Loss, Spin-orbit interaction and anomalous spin relaxation in carbon nanotube quantum dots, *Physical Review B* **77**, 235301 (2008).
- [16] E. A. Laird, F. Kuemmeth, G. A. Steele, K. Grove-Rasmussen, J. Nygård, K. Flensberg, and L. P. Kouwenhoven, Quantum transport in carbon nanotubes, *Reviews of Modern Physics* **87**, 703 (2015).
- [17] E. A. Laird, F. Pei, and L. P. Kouwenhoven, A valley-spin qubit in a carbon nanotube, *Nature Nanotechnology* **8**, 565 (2013).
- [18] T. Pei, A. Pályi, M. Mergenthaler, N. Ares, A. Mavalankar, J. H. Warner, G. A. D. Briggs, and E. A. Laird, Hyperfine and Spin-Orbit Coupling Effects on Decay of Spin-Valley States in a Carbon Nanotube, *Physical Review Letters* **118**, 177701 (2017).
- [19] A. Cottet and T. Kontos, Spin Quantum Bit with Ferromagnetic Contacts for Circuit QED, *Physical Review Letters* **105**, 160502 (2010).
- [20] T. Cubaynes, L. C. Contamin, M. C. Dartiailh, M. M. Desjardins, A. Cottet, M. R. Delbecq, and T. Kontos, Nanoassembly technique of carbon nanotubes for hybrid circuit-QED, *Applied Physics Letters* **117**, 114001 (2020).
- [21] B. Undseth, O. Pietx-Casas, E. Raymenants, M. Mehmandoost, M. T. Mađzik, S. G. J. Philips, S. L. de Snoo, D. J. Michalak, S. V. Amitonov, L. Tryputen, B. P. Wuetz, V. Fezzi, D. D. Esposti, A. Sammak, G. Scappucci, and L. M. K. Vandersypen, Hotter is Easier: Unexpected Temperature Dependence of Spin Qubit Frequencies, *Physical Review X* **13**, 041015 (2023).
- [22] L. Petit, H. G. J. Eenink, M. Russ, W. I. L. Lawrie, N. W. Hendrickx, S. G. J. Philips, J. S. Clarke, L. M. K. Vandersypen, and M. Veldhorst, Universal quantum logic in hot silicon qubits, *Nature* **580**, 355 (2020).
- [23] C. H. Yang, R. C. C. Leon, J. C. C. Hwang, A. Saraiva, T. Tanttu, W. Huang, J. Camirand Lemyre, K. W. Chan, K. Y. Tan, F. E. Hudson, K. M. Itoh, A. Morello, M. Pioro-Ladrière, A. Laucht, and A. S. Dzurak, Operation of a silicon quantum processor unit cell above one kelvin, *Nature* **580**, 350 (2020).
- [24] S. Sahoo, T. Kontos, J. Furer, C. Hoffmann, M. Gräber, A. Cottet, and C. Schönenberger, Electric field control of spin transport, *Nature Physics* **1**, 99 (2005).
- [25] A. Théry, B. Neukelmance, B. Hue, W. Legrand, L. Jarjat, J. Craquelin, M. Villiers, A. Cottet, M. R. Delbecq, and T. Kontos, Observation of quantum oscillations in the extreme weak anharmonic limit, *Physical Review B* **109**, 064505 (2024).
- [26] J. Claudon, A. Zazunov, F. W. J. Hekking, and O. Buisson, Rabi-like oscillations of an anharmonic oscillator: Classical versus quantum interpretation, *Physical Review B* **78**, 184503 (2008).
- [27] J. J. Viennot, M. R. Delbecq, M. C. Dartiailh, A. Cottet, and T. Kontos, Out-of-equilibrium charge dynamics in a hybrid circuit quantum electrodynamics architecture, *Physical Review B* **89**, 165404 (2014).
- [28] L. E. Bruhat, T. Cubaynes, J. J. Viennot, M. C. Dartiailh, M. M. Desjardins, A. Cottet, and T. Kontos, Circuit QED with a quantum-dot charge qubit dressed by Cooper pairs, *Physical Review B* **98**, 155313 (2018).
- [29] M. Delbecq, *Spin Quantum Dynamics in Hybrid Circuits*,

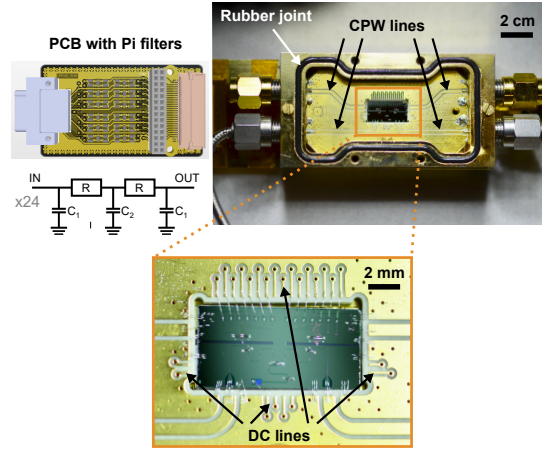
Habilitation thesis, Sorbonne Université (2020).

- [30] E. Mariani and F. von Oppen, Electron-vibron coupling in suspended carbon nanotube quantum dots, *Physical Review B* **80**, 155411 (2009).
- [31] U. Hartmann and F. Wilhelm, Decoherence of Charge States in Double Quantum Dots Due to Cotunneling, *physica status solidi (b)* **233**, 385 (2002).
- [32] K. Takeda, J. Kamioka, T. Otsuka, J. Yoneda, T. Nakajima, M. R. Delbecq, S. Amaha, G. Allison, T. Kodera, S. Oda, and S. Tarucha, A fault-tolerant addressable spin qubit in a natural silicon quantum dot, *Science Advances* **2**, e1600694 (2016).
- [33] J. J. Viennot, M. C. Dartiailh, A. Cottet, and T. Kontos, Coherent coupling of a single spin to microwave cavity photons, *Science* **349**, 408 (2015).
- [34] A. Cottet and T. Kontos, Spin Quantum Bit with Ferromagnetic Contacts for Circuit QED, *Physical Review Letters* **105**, 160502 (2010).
- [35] A. Cottet, M. C. Dartiailh, M. M. Desjardins, T. Cubaynes, L. C. Contamin, M. Delbecq, J. J. Viennot, L. E. Bruhat, B. Douçot, and T. Kontos, Cavity QED with hybrid nanocircuits: From atomic-like physics to condensed matter phenomena, *Journal of Physics: Condensed Matter* **29**, 433002 (2017).

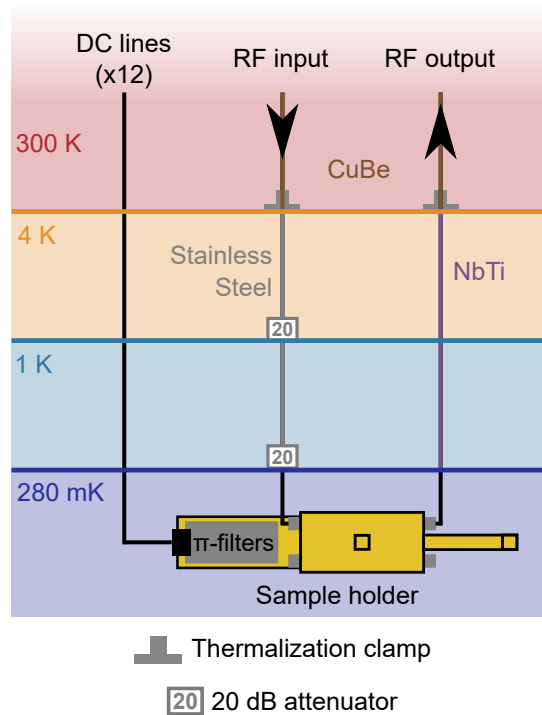
# Supplementary materials for "Microsecond-lived quantum states in a carbon-based circuit driven by cavity photons"

## S1. MATERIALS AND METHODS

### A. Wiring

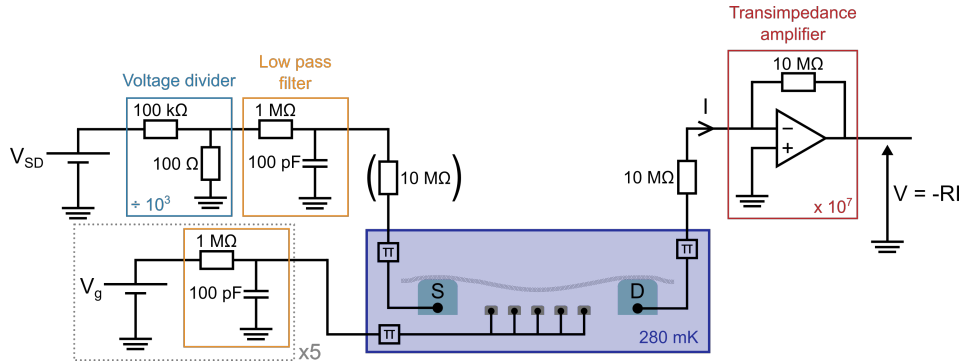


Supplementary Figure 1. **Circuit chip embedded in the sampler holder.** The PCB contains 24 DC lines and 4 CPW lines for RF signals. Each DC line has a Pi filter:  $R = 1 \text{ k}\Omega$ ,  $C_1 = 1 \text{ nF}$  and  $C_2 = 2.2 \text{ nF}$ . A rubber joint ensures the vacuum tightness when closing the sample holder with its cover inside the stapler.



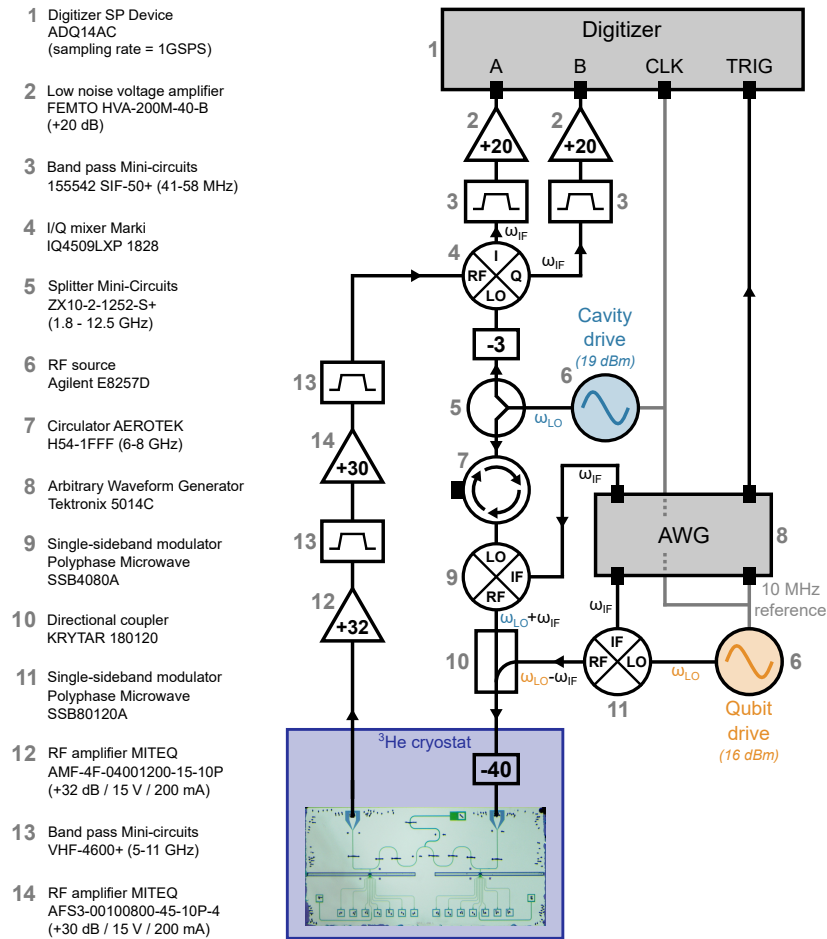
Supplementary Figure 2.  **$^3\text{He}$  cryostat wiring.** The attenuators thermalize both the outer and inner part of the coaxial cables and reduce thermal noise. The NbTi line provides very few attenuation to the RF output line.

### B. DC measurements



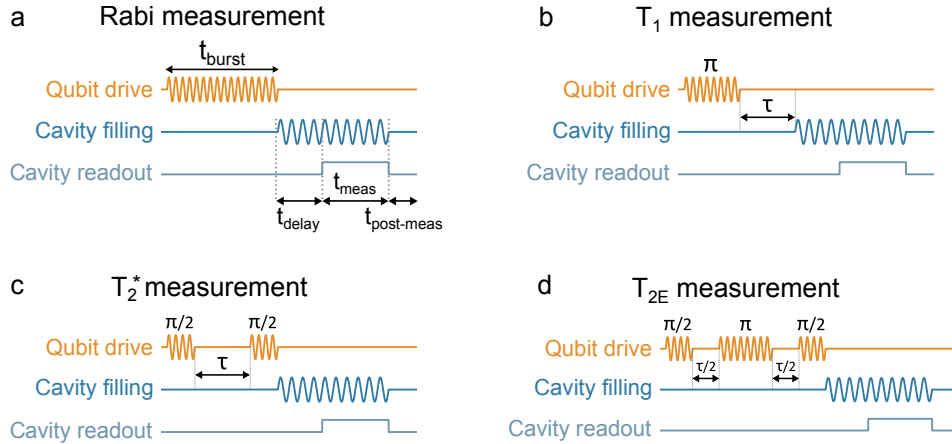
Supplementary Figure 3. **DC measurements set-up.** The voltage divider reduces the bias voltage  $V_{SD}$  by a factor of  $10^3$ . The current going out of the cryostat is amplified by a factor  $10^7$  by a low noise I-V converter.

### C. RF measurements



Supplementary Figure 4. **RF measurements set-up.**

### D. Pulse sequences for the RF time domain measurements

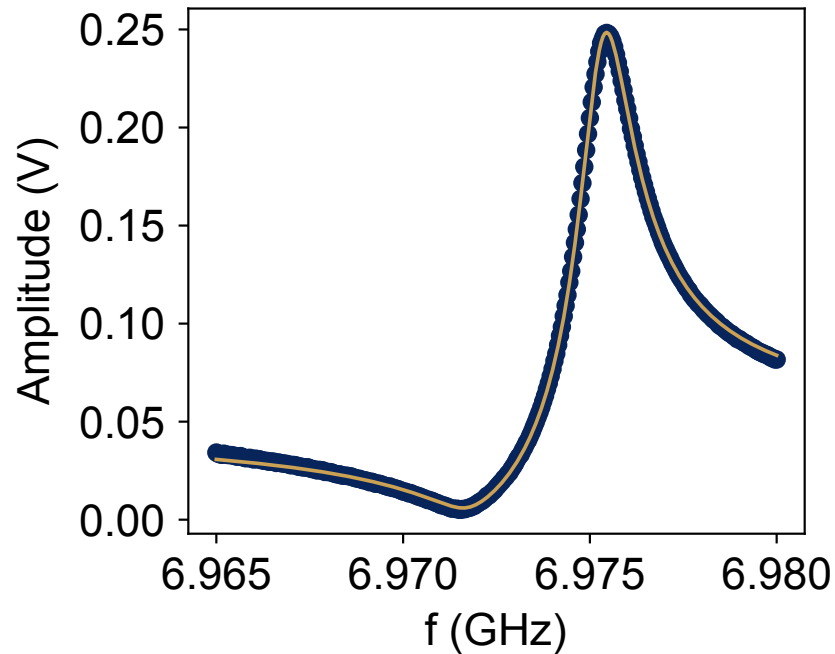


Supplementary Figure 5. **Pulse sequences.**

For each RF time domain measurement presented in the paper, the cavity is measured during  $t_{meas} = 600$  ns after a delay time  $t_{delay} = 250$  ns, such that in total the cavity is filled during  $t_{delay} + t_{meas} = 850$  ns. We add a post-measuring time  $t_{post-meas} = 3$   $\mu$ s to let both the cavity and the transitions relax in their ground state after the measurement. In order to average the signal acquired, each pulse sequence is repeated  $N_{avg} = 150\,000$  times. For the Rabi measurements,  $t_{burst}$  is varied from 0  $\mu$ s to 2  $\mu$ s by steps of 20 ns. For the  $T_1$  measurement  $\tau$  is varied from 0  $\mu$ s to 5  $\mu$ s by steps of 20 ns. For the  $T_2^*$  and  $T_{2E}$  measurements  $\tau$  is varied from 0  $\mu$ s to 2  $\mu$ s by steps of 20 ns. A  $\pi$ -pulse is achieved in 200 ns, so logically a  $\pi/2$ -pulse is achieved in 100 ns.

## S2. ADDITIONAL EXPERIMENTAL DATA

### A. Cavity resonance



Supplementary Figure 6. **Cavity resonance.** The filled circles are the data and solid orange line is the fit.

The cavity is fitted with  $|S_{21}|$  and  $S_{21}$  is defined as follows:

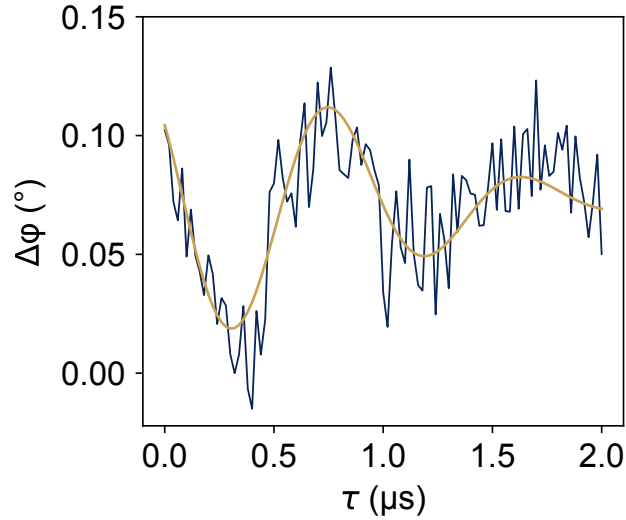
$$S_{21} = \frac{\sqrt{\kappa_{in}\kappa_{out}}}{i2\pi(f_c - f) + \kappa/2} + i\sqrt{T}e^{i\zeta} \quad (S1)$$

where  $f_c$  is resonance frequency of the cavity,  $\kappa$  is the linewidth of the cavity,  $\kappa_{in}$  and  $\kappa_{out}$  are respectively the couplings to the input and output ports of the cavity,  $f$  is driving frequency, and  $T$  and  $\zeta$  are Fano parameters.

Parameters	Values
$f_c$	6.975 GHz
$\kappa$	1.437 MHz
$\sqrt{\kappa_{in}\kappa_{out}}$	174.311 kHz
$T$	0.00226699
$\zeta$	317.369467

Supplementary Table I. Fit parameters for the cavity resonance

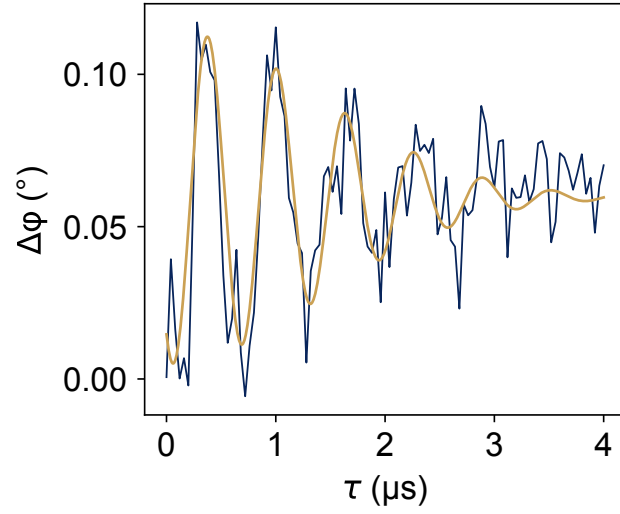
### B. Ramsey oscillations



Supplementary Figure 7. **Ramsey oscillations**

These Ramsey oscillations are obtained by driving at 9.0986 GHz. The blue line represents the data and the solid yellow line is a fit with a Gaussian decaying cosine. It yields  $T_2^* = (1.27 \pm 0.15) \mu\text{s}$ .

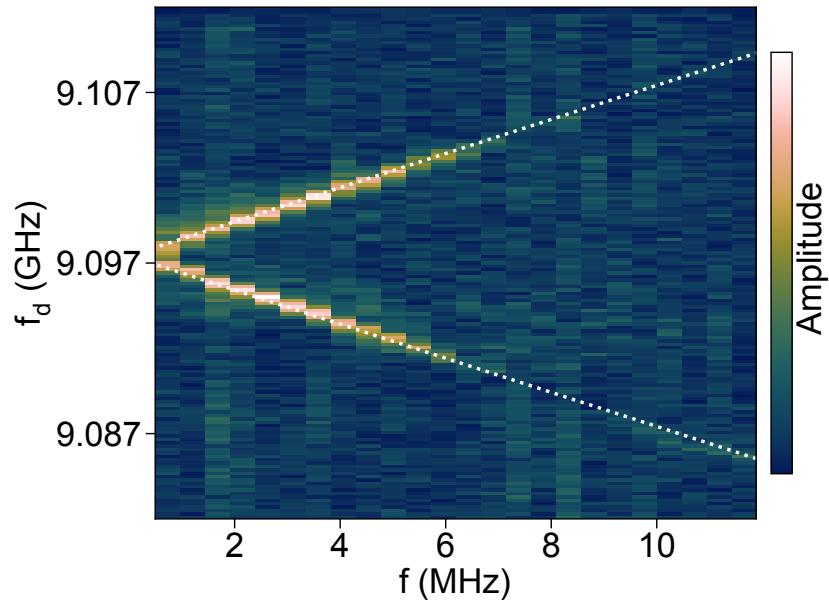
### C. Hahn-echo oscillations



Supplementary Figure 8. **Hahn-echo oscillations**

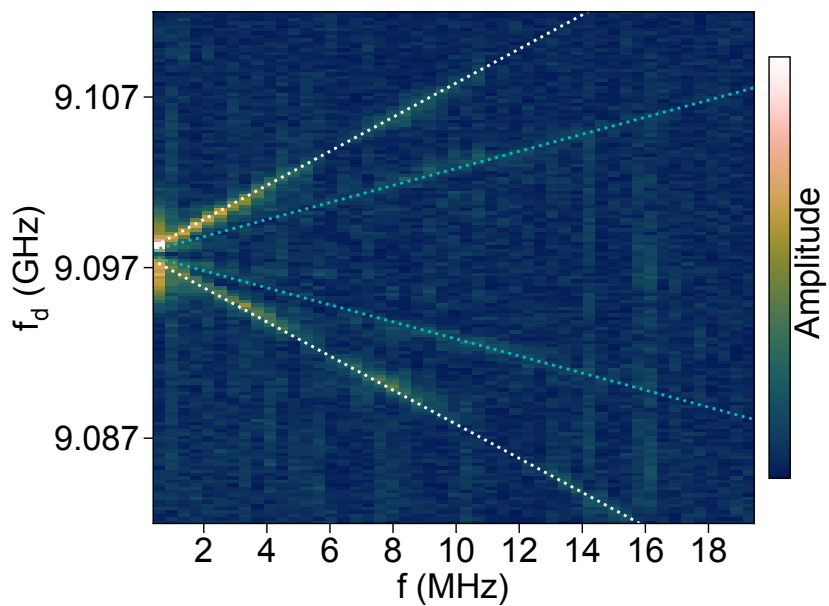
These Hahn-echo oscillations are obtained by driving at 9.1010 GHz. The blue line represents the data and the solid yellow line is a fit with a Gaussian decaying cosine. It yields  $T_{2E} = (2.02 \pm 0.21) \mu\text{s}$ .

### D. Fourier transform of the Ramsey fringes



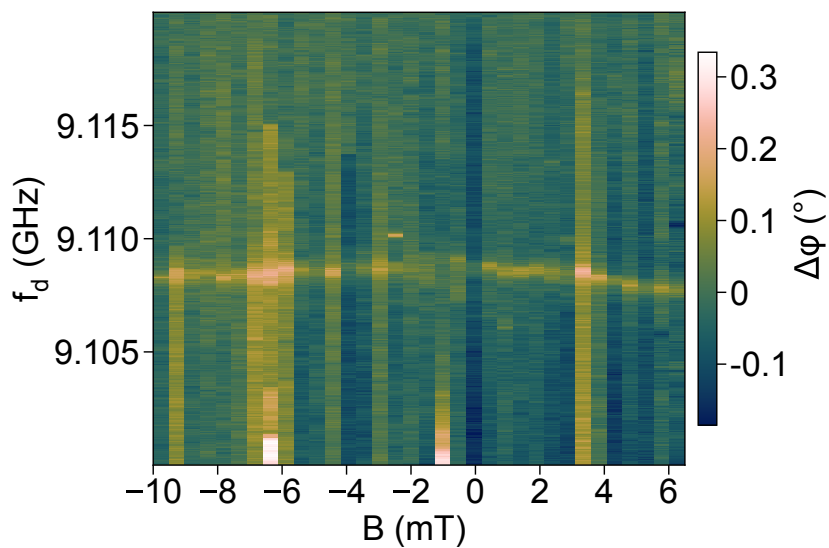
Supplementary Figure 9. **Fourier transform of the Ramsey fringes.** The white dashed line plots the following formula :  $|f - f_0|$  with  $f_0 = 9.0974$  GHz. We do observe that the oscillations frequency depends linearly on the drive frequency detuning.

### E. Fourier transform of the Hahn-echo fringes



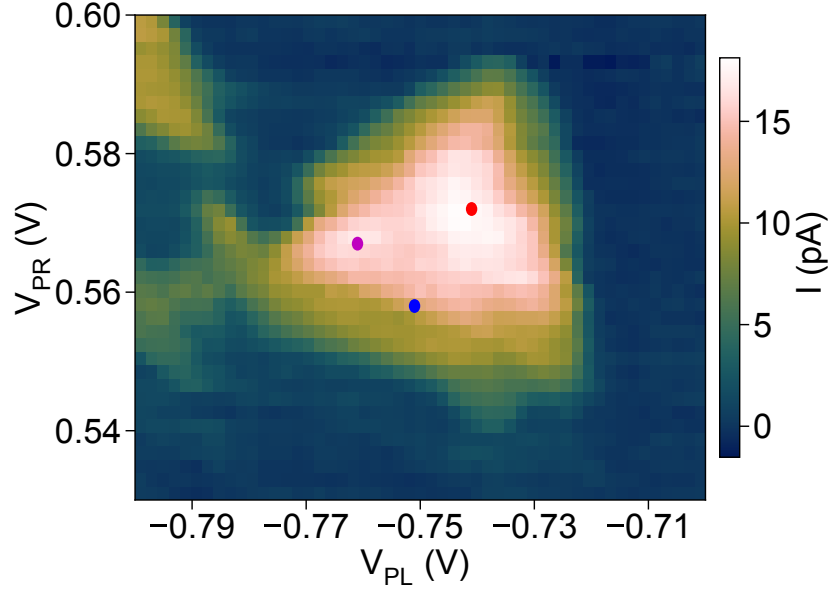
Supplementary Figure 10. **Fourier transform of the Hahn-echo fringes.** The white dashed lined plots  $|f - f_0|$  and the blue dashed lined plots  $2 \times |f - f_0|$ , both with  $f_0 = 9.0978$  GHz.

### F. Magnetic field dispersion



Supplementary Figure 11. **Magnetic field dispersion.**

### G. Working points for magnetoresistance experiment



Supplementary Figure 12. **Working points for magnetoresistance experiment.** The red dot shows the working point for the upper pair of curves in figure 1B, the purple dot shows the working point for the middle pair of curves in figure 1B, and blue dot shows the working point for the lower pair of curves in figure 1B. The bias triangles are measured at  $V_{SD} = 10$  mV.

### S3. SINGLE PARTICLE DQD HAMILTONIAN COUPLED TO A CAVITY MODE

The simulations presented in the main text are based on microscopic modelling of the CNT based double quantum dot circuit coupled to microwave photons [33].

#### A. The DQD-cavity Hamiltonian

The Hamiltonian of the coupled system is

$$\hat{H} = \hat{H}_{\text{cav}} + \hat{H}_{\text{int}} + \hat{H}_{\text{DQD}}. \quad (\text{S2})$$

The cavity Hamiltonian is

$$\hat{H}_{\text{cav}} = \hbar\omega_c \hat{a}^\dagger \hat{a} \quad (\text{S3})$$

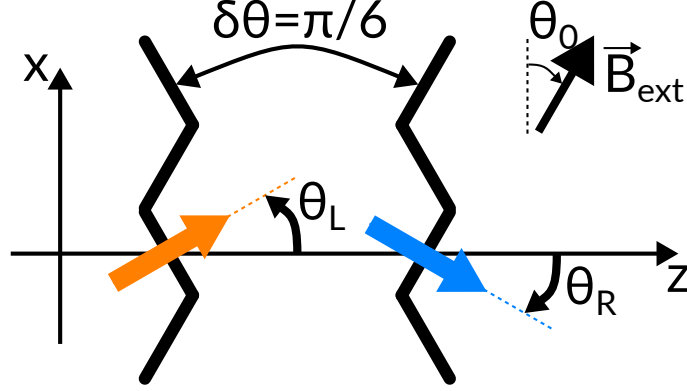
with  $\omega_c/(2\pi)$  the cavity frequency and  $\hat{a}$  ( $\hat{a}^\dagger$ ) the creation (annihilation) operator of a photon in the cavity mode.

We restrict the Hamiltonian  $\hat{H}_{\text{DQD}}$  of the CNT double quantum dot with non-collinear ferromagnetic contacts to single particle occupancy. We consider the two valleys  $K$  and  $K'$  in the description. The exchange interaction in the ferromagnetic leads induce effective Zeeman fields  $\vec{E}_{L/R,K/K'}^Z$  which can be different in both dots (due to different contacts) and can differ from  $K$  to  $K'$ . The double quantum dot Hamiltonian reads

$$\begin{aligned} \hat{H}_{\text{DQD}} = & -\frac{1 + \hat{\tau}_z}{2} \left[ \frac{\vec{E}_{L,K}^Z (1 + \hat{\gamma}_z) + \vec{E}_{L,K'}^Z (1 - \hat{\gamma}_z) + g_L \mu_B \vec{B}_{\text{ext}}}{2} \right] \cdot \vec{\sigma} \\ & -\frac{1 - \hat{\tau}_z}{2} \left[ \frac{\vec{E}_{R,K}^Z (1 + \hat{\gamma}_z) + \vec{E}_{R,K'}^Z (1 - \hat{\gamma}_z) + g_R \mu_B \vec{B}_{\text{ext}}}{2} \right] \cdot \vec{\sigma} \\ & + \frac{1}{2} [\Delta_{L,KK'} (1 + \hat{\gamma}_z) + \Delta_{R,KK'} (1 - \hat{\gamma}_z)] \\ & + (t_c \hat{\tau}_x + \epsilon_\delta \hat{\tau}_z) \hat{\gamma}_0 \hat{\sigma}_0 - \frac{1}{2} g_{\text{orb}} \mu_B (\vec{B}_{\text{ext}} \cdot \vec{u}_z) \hat{\gamma}_z \hat{\tau}_0 \hat{\sigma}_0, \end{aligned} \quad (\text{S4})$$

with  $\vec{E}_{L/R,K/K'}^Z = E_{L/R,K/K'}^Z [\cos(\theta_{L/R})\vec{u}_z + \sin(\theta_{L/R})\vec{u}_x]$ , where  $\vec{u}_x$ ,  $\vec{u}_z$  are units vectors along the  $x$  and  $z$  directions, the  $z$  directions being chosen along the CNT axis and  $\theta_{L/R}$  is the angle between the L/R contact magnetization and the  $z$  direction. The parametrization of the angles is described in Fig. 13, giving  $\theta_{L/R} = \frac{1}{2}(\pi - \delta\theta)$  where  $\delta\theta$  is the angle between the zig-zags of the ferromagnetic contacts, fixed by design to  $\delta\theta = \pi/6$ .

In  $\hat{H}_{\text{DQD}}$ ,  $\hat{\sigma}_i$ ,  $\hat{\gamma}_i$ ,  $\hat{\tau}_i$  with  $i \in \{0, x, y, z\}$  are the Pauli matrices operators acting in the spin space, the valley space and the L/R space of the double quantum dot respectively, with index 0 giving the identity matrix in the corresponding subspace. The Landé g-factors  $g_{L/R}$  can in principle be different on both dots, although we fix them equal to 2 in both dots in the following,  $\mu_B$  is the Bohr magneton,  $\vec{B}_{\text{ext}}$  is the external magnetic field,  $g_{\text{orb}}$  the orbital g-factor. We account for valley mixing  $\Delta_{L/R, KK'}$  which can differ in both dots due to spatially varying disorder or curvature of the suspended CNT. Finally the tunnel coupling between the two dots is  $t_c$  and the energy detuning between the two levels in each dot is  $\epsilon_\delta$ .



Supplementary Figure 13. Schematic representation of the device showing the the angle parametrizations. The ferromagnetic contacts magnetizations are displayed as orange (left contact) and blue (right contact) arrows making an angle  $\theta_L$  and  $\theta_R$  with the  $z$ -axis respectively. The angle between the contacts zig-zag is  $\delta\theta = \pi/6$  designed by EB lithography (see figure 1 of the main text). The external magnetic field  $\vec{B}_{\text{ext}}$  has an angle  $\theta_0$  with respect to the  $x$ -axis to account for possible misalignment.

The coupling Hamiltonian between the cavity and the DQD is

$$\hat{H}_{\text{int}} = \hbar g_0 (\hat{a} + \hat{a}^\dagger) \hat{\tau}_z \hat{\gamma}_0 \hat{\sigma}_0, \quad (\text{S5})$$

where  $g_0$  is the bare electron-photon coupling strength.

To reproduce both the dispersion with  $\epsilon_\delta$  and the time domain measurements, we used two sets of parameters that are close to each other (see table II). This is motivated by the fact that over the measurement run the frequencies slightly shifted. Then we adjust the spectrum to match the transitions frequencies at zero detuning  $\epsilon_\delta = 0$  and their dispersion in detuning  $\epsilon_\delta$  as well as the couplings of each transition to cavity photon to account for the contrast of the Rabi chevrons. The couplings to each transition is  $g_{ij} = g_0 \langle i | \hat{\tau}_z \hat{\gamma}_0 \hat{\sigma}_0 | j \rangle$  where  $|i\rangle$  and  $|j\rangle$  are eigenstates corresponding to eigenvalues of levels  $i$  and  $j$ . With this set of parameters, the couplings matrix  $\langle i | \hat{\tau}_z \hat{\gamma}_0 \hat{\sigma}_0 | j \rangle$  at zero detuning  $\epsilon_\delta = 0$  is:

$$\begin{pmatrix} 0 & 2.4 \times 10^{-3} & 8.52 \times 10^{-2} & 9.2 \times 10^{-3} & 9.9632 \times 10^{-1} & 1.9 \times 10^{-3} & 6 \times 10^{-5} & 0 \\ 2.4 \times 10^{-3} & 0 & 2.5 \times 10^{-3} & 8.52 \times 10^{-2} & 1.4 \times 10^{-3} & 9.9636 \times 10^{-1} & 0 & 6 \times 10^{-5} \\ 8.52 \times 10^{-2} & 2.5 \times 10^{-3} & 0 & 2.4 \times 10^{-3} & 3 \times 10^{-5} & 0 & 9.9632 \times 10^{-1} & 1.9 \times 10^{-3} \\ 9.2 \times 10^{-3} & 8.52 \times 10^{-2} & 2.4 \times 10^{-3} & 0 & 0 & 3 \times 10^{-5} & 1.4 \times 10^{-3} & 9.9632 \times 10^{-1} \\ 9.9632 \times 10^{-1} & 1.4 \times 10^{-3} & 3 \times 10^{-5} & 0 & 0 & 2.4 \times 10^{-3} & 8.52 \times 10^{-2} & 9.2 \times 10^{-3} \\ 1.9 \times 10^{-3} & 9.9636 \times 10^{-1} & 0 & 3 \times 10^{-5} & 2.4 \times 10^{-3} & 0 & 2.5 \times 10^{-3} & 8.52 \times 10^{-2} \\ 6 \times 10^{-5} & 0 & 9.9636 \times 10^{-1} & 1.4 \times 10^{-3} & 8.52 \times 10^{-2} & 2.5 \times 10^{-3} & 0 & 2.4 \times 10^{-3} \\ 0 & 6 \times 10^{-5} & 1.9 \times 10^{-3} & 9.9632 \times 10^{-1} & 9.2 \times 10^{-3} & 8.52 \times 10^{-2} & 2.4 \times 10^{-3} & 0 \end{pmatrix} \quad (\text{S6})$$

With this, we have the Rabi frequencies of the three transitions of the quasi-harmonic ladder given by  $\Omega_{01} = \Omega_{23} = 2.65$  MHz and  $\Omega_{12} = 2.8$  MHz, obtained by multiplying the corresponding coupling term by drive amplitude term of value 40.7 common to all three transitions. The transition frequencies defined by  $f_{ij} = (E_j - E_i)/h$  are  $f_{01} = 9098.0$  MHz,  $f_{12} = 9096.1$  MHz and  $f_{23} = 9096.0$  MHz.

Fixed Parameters		Adjusted Parameters for the dispersion with $\epsilon_\delta$		Adjusted Parameters for the time domain measurements	
$\delta\theta$	$\pi/6$	$\Delta_{L,KK'}/h$	4541.2 MHz	$\Delta_{L,KK'}/h$	4543.9 MHz
$\frac{1}{2}g_L\mu_B$	28000 MHz T <sup>-1</sup>	$\Delta_{R,KK'}/h$	4529.8 MHz	$\Delta_{R,KK'}/h$	4534.7 MHz
$\frac{1}{2}g_R\mu_B$	28000 MHz T <sup>-1</sup>	$E_{L,K}^Z/h$	9656.7 MHz	$E_{L,K}^Z/h$	9690.1 MHz
		$E_{L,K'}^Z/h$	9189.9 MHz	$E_{L,K'}^Z/h$	9222.1 MHz
		$E_{R,K}^Z/h$	9825.6 MHz	$E_{R,K}^Z/h$	9814.6 MHz
		$E_{R,K'}^Z/h$	9043.7 MHz	$E_{R,K'}^Z/h$	9069.7 MHz
$\omega_c/(2\pi)$	6975 MHz	$g_0/(2\pi)$	27.0 MHz	$g_0/(2\pi)$	27.0 MHz
$\kappa$	1.44 MHz	$t_c/h$	41020 MHz	$t_c/h$	31190.0 MHz

Supplementary Table II. Parameters of the Hamiltonian in MHz used for numerical calculations.

## B. Dephasing and relaxation

The dephasing is taken into account following the discussion in the supplementary material of ref. [34]. Dephasing for each degree of freedom (charge left/right, spin up/down and valley K/K') is calculated with perturbation theory. For spin and valley, we restrict ourselves to first order while for charge we go to second order to deal with sweet spots where the first order derivative cancels. We have

$$\Gamma_{\varphi,ij}^s/(2\pi) = \sqrt{A_s^2 |\langle j | \hat{\tau}_0 \hat{\gamma}_0 \hat{\sigma}_z | j \rangle - \langle i | \hat{\tau}_0 \hat{\gamma}_z \hat{\sigma}_0 | i \rangle|^2} \quad (S7)$$

$$\Gamma_{\varphi,ij}^v/(2\pi) = \sqrt{A_v^2 |\langle j | \hat{\tau}_0 \hat{\gamma}_0 \hat{\sigma}_z | j \rangle - \langle i | \hat{\tau}_0 \hat{\gamma}_z \hat{\sigma}_0 | i \rangle|^2} \quad (S8)$$

$$\Gamma_{\varphi,ij}^c/(2\pi) = \sqrt{A_c^2 |\langle j | \hat{\tau}_0 \hat{\gamma}_0 \hat{\sigma}_z | j \rangle - \langle i | \hat{\tau}_0 \hat{\gamma}_0 \hat{\sigma}_z | i \rangle|^2 + \left[ \sum_k \frac{|\langle k | \hat{\tau}_0 \hat{\gamma}_0 \hat{\sigma}_z | j \rangle|^2}{E_k - E_j} - \sum_{k'} \frac{|\langle k' | \hat{\tau}_0 \hat{\gamma}_0 \hat{\sigma}_z | i \rangle|^2}{E_{k'} - E_j} \right]^2} A_c^4 \quad (S9)$$

For combining the dephasing rates associated with each derivative for charge noise we choose the ansatz of computing the square root of the sum of the squares of each contributions. The total dephasing rate for each transition is then the sum of the three contributions  $\Gamma_{\varphi,ij} = \Gamma_{\varphi,ij}^s + \Gamma_{\varphi,ij}^v + \Gamma_{\varphi,ij}^c$ . The parameters  $A_\alpha$  for  $\alpha = \{s, v, c\}$  correspond to the amplitude of fluctuations of the parameters controlling the dephasing. For charge noise it corresponds to the amplitude of fluctuations of the detuning  $A_c = \sqrt{\langle \epsilon_\delta \rangle^2}$ . For spin dephasing,  $A_s$  comprises contributions from the nuclear spins environment and from the fluctuations of the exchange fields. For reproducing the experimental data, we take  $A_c = 250$  MHz,  $A_s < 10$  MHz and  $A_v = 0.2$  MHz. We note that the value of  $A_c$  corresponds to fluctuations of the detuning of standard deviation  $\sqrt{\langle \epsilon_\delta \rangle^2} \approx 1$   $\mu$ eV which is an indication of a very low charge noise, as expected for an ultra-clean carbon nanotube. In the main text however, we keep a more conservative value of  $\sqrt{\langle \epsilon_\delta \rangle^2} \approx 10$   $\mu$ eV to estimate the amplitude of charge noise because we lack independent experimental confirmation of the low detuning fluctuations. The dephasing rates matrix restricted to the relevant subspace  $\{|0\rangle, |1\rangle, |2\rangle, |3\rangle\}$  for the dynamics of our system reads in MHz

$$\Gamma_{\varphi}/(2\pi) = \begin{pmatrix} & 0.029 & 0.158 & 0.129 \\ 0.029 & & 0.137 & 0.157 \\ 0.158 & 0.137 & & 0.030 \\ 0.129 & 0.157 & 0.030 & \end{pmatrix} \quad (S10)$$

For relaxation in the simulations, we consider phonons. At the transition frequency  $\sim 9$  GHz, the relevant modes are stretching modes which have a fundamental mode frequency  $\nu_0$  given by the relation  $\nu_0 L = 12.3$  GHz  $\cdot \mu$ m with  $L$  the length of the CNT in  $\mu$ m [30]. Due to the nanoassembly technique, we do not know exactly the location of the CNT along the gates. Depending on its location on the zig-zag contacts, the length of the CNT suspended over the gate electrodes varies typically between 1.5 and 2  $\mu$ m giving  $\nu_0$  between 8.2 and 6.15 GHz. Relaxation is accounted for by a radiative Purcell process. As we work at a temperature comparable to the transitions frequencies, the thermal

occupancy  $n_{ij}^{\text{th}}$  is non vanishing, hence inverse Purcell effect which excite lower states to higher states are non zero and must be taken into account. We have

$$\Gamma_{1,ij}^{\downarrow}/(2\pi) = \kappa_{\nu}/(2\pi) \left( \frac{g_{ij}^{\nu}/\sqrt{n}}{\nu_n - f_{ij}} \right)^2 (n_{ij}^{\text{th}} + 1) \quad (\text{S11})$$

$$\Gamma_{1,ij}^{\uparrow}/(2\pi) = \kappa_{\nu}/(2\pi) \left( \frac{g_{ij}^{\nu}/\sqrt{n}}{\nu_n - f_{ij}} \right)^2 n_{ij}^{\text{th}} \quad (\text{S12})$$

with  $\nu_n = n\nu_0$  the frequency of the  $n$ -th harmonic and  $n_{ij}^{\text{th}} = \frac{1}{e^{hf_{ij}/k_B T} - 1}$ . Here we take the scaling that the charge-phonon coupling  $g_{ij}^{\nu}$  scales as  $1/\sqrt{n}$  [30]. The charge-phonon coupling matrix elements are the same as the charge-photon matrix elements given in (S6). The bare charge-phonon coupling  $g_0^{\nu}$  is however different than the bare charge-photon coupling.  $g_0^{\nu}$  is expected to be large and is a free parameter in the model. The phonon mode damping rate  $\kappa_{\nu}$  is the third free parameter and as its scaling with the harmonic number is not clearly predicted, we kept it constant. For the simulation we considered up to  $n = 5$  harmonics so that all transitions of the quasi-harmonic ladder have a contribution. Varying the length  $L$  of the CNT, we find that to reproduce the data, we have very similar relaxation matrix with  $\Gamma_{1,02}^{\downarrow}$  and  $\Gamma_{1,13}^{\downarrow}$  dominating the relaxation process. Restricting again to the  $\{|0\rangle, |1\rangle, |2\rangle, |3\rangle\}$  subspace, the relaxation matrix for  $L = 1.5 \mu\text{m}$ ,  $g_0^{\nu} = 500 \text{ MHz}$  and  $\kappa_{\nu} = 2.5 \text{ GHz}$  is in MHz

$$\Gamma_1/(2\pi) = \begin{pmatrix} & 6 \times 10^{-3} & 8.4 \times 10^{-1} & 3 \times 10^{-3} \\ 1 \times 10^{-3} & & 7 \times 10^{-3} & 8.4 \times 10^{-1} \\ 4.6 \times 10^{-2} & 2 \times 10^{-3} & & 6 \times 10^{-3} \\ 4 \times 10^{-5} & 4.6 \times 10^{-2} & 1 \times 10^{-3} & \end{pmatrix} \quad (\text{S13})$$

The parameters used to compute the dephasing and relaxation rates for the simulation of the Rabi chevron and the Ramsey fringes presented in the main text are summarized in table III

Dephasing		Relaxation	
$A_c$	250 MHz	$g_0^{\nu}$	500 MHz
$A_s$	10 MHz	$\kappa_{\nu}$	2500 MHz
$A_v$	0.2 MHz	$L$	1.5 $\mu\text{m}$

Supplementary Table III. Parameters used to calculate the dephasing and relaxation rates.

### C. Cavity readout

The transmission  $S_{21}$  of microwave field through the dqd-cavity system is given by [35]:

$$S_{21} = \frac{\sqrt{\kappa_1 \kappa_2}}{\Delta_{\text{cd}} - i \frac{\kappa}{2} - \Xi}, \quad (\text{S14})$$

with  $\Delta_{\text{cd}} = \omega_c - \omega_d$  the detuning between the cavity and the drive angular frequencies,  $\kappa/(2\pi)$  the cavity linewidth. The total susceptibility  $\Xi$  is given by

$$\Xi = \sum_{ij} \frac{g_{ij}^2 (n_j - n_i)}{\omega_{ij} - \omega_d - i \frac{\Gamma_{ij}}{2}}, \quad (\text{S15})$$

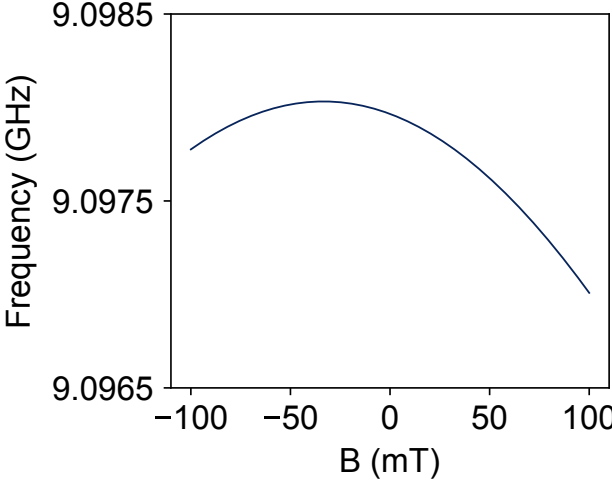
with  $n_{i,j}$  the population of level  $i, j$ ,  $\omega_{ij} = (E_j - E_i)/\hbar$  are transitions angular frequencies and  $\Gamma_{ij}$  is the decoherence rate associated with the transition between states  $|i\rangle$  and  $|j\rangle$  given by  $\Gamma_{ij} = \frac{\Gamma_{1,ij}}{2} + \Gamma_{\varphi,ij}$ . The thermal equilibrium populations are given by the Boltzmann weight

$$n_i = \frac{e^{-E_i/k_B T}}{\sum_k e^{-E_k/k_B T}}, \quad (\text{S16})$$

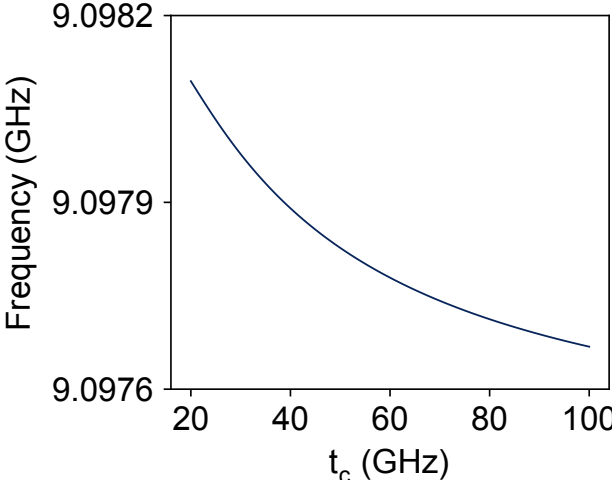
with  $E_i$  the energy of the  $i$ -th level. In this work we have  $T = 300 \text{ mK}$ . For simulations of the Rabi and Ramsey experiments, the initial state is the thermal equilibrium state  $\{0.77, 0.18, 0.04, 0.01, 0, 0, 0, 0\}$ . The calculated populations at each evolution time are then used in equation (S14) to calculate the phase of the cavity field. To reproduce

the phase contrast observed experimentally, we have to manually change a single parameter from the value computed from the Hamiltonian. This parameter is  $g_{03}$  which must be increased by a factor approximately 40. We checked that using this value to calculate the relaxation rates due to phonons reproduces the same simulation given that we slightly reduce  $\kappa_\nu$  to 1.5 GHz. This highlights that parameters used to compute the relaxation rates with phonons are not discriminant.

D. Simulated dispersions



Supplementary Figure 14. **Simulated dispersion of the 01 transition frequency with respect to the external magnetic field.** It is computed with the parameters used to reproduce the time domain measurement.



Supplementary Figure 15. **Simulated dispersion of the 01 transition frequency with respect to the interdot tunnel coupling.** It is computed with the parameters used to reproduce the time domain measurement.